(Received 12 January 2026, Accepted 30 January 2026, Scheduled 14 February 2026)

Sensorless Control of PMSM Based on a Novel Nonlinear Sliding Mode Observer with Phase-Locked Loop

Kun Wang[1], Zhonggen Wang[1,*], and Wenyan Nie[2]

[1] School of Electrical and Information Engineering, Anhui University of Science and Technology, Huainan 232001, China
[2] School of Mechanical and Electrical Engineering, Huainan Normal University, Huainan 232001, China

ABSTRACT: To improve the position detection accuracy of sensorless control for permanent magnet synchronous motors (PMSM) and address issues such as significant chattering amplitude in the traditional Sliding Mode Observers (SMOs), a Novel Adaptive Nonlinear Super-Twisting Sliding Mode Observer (NANSTSMO) combined with a Higher-order Gain Compensation Phase-Locked Loop (HGC-PLL) is designed in this study. First, a multimodal nonlinear function is designed to replace the sign switching function, and this multimodal nonlinear function is then integrated with both the NANSTSMO and HGCPLL. Second, a compensation mechanism is introduced to precisely estimate the rotor position. Finally, simulations are conducted using MATLAB/Simulink, and a motor test platform is constructed. Compared with the traditional sliding mode control and referenced sliding mode control strategies, the proposed method demonstrates superior effectiveness.

1. INTRODUCTION

Permanent magnet synchronous motors (PMSMs) are widely adopted in high-traction power applications, such as new energy vehicles [1], rail transit systems [2], and robotics [3], because of their high power density, compact size, and large output torque. High-performance PMSM control typically utilizes mechanical sensors to obtain information, such as rotor position. However, the associated sensor equipment increases cost [4]. Therefore, sensorless control is considered an effective solution.

At present, sensorless control strategies for PMSM are primarily categorized into methods based on high-frequency signal injection [5] and those based on the fundamental wave mathematical model [6]. Among them, the high-frequency signal injection method is mainly suitable for low-speed and zero-speed operations, whereas the fundamental wave model method is primarily applicable to medium-high speeds. The latter relies on the back electromotive force (back-EMF) from the fundamental excitation mathematical model of the PMSM for rotor position and speed estimation. To obtain accurate back-EMF information, many advanced control methods have been proposed, such as the sliding mode observer (SMO) algorithm [7], sliding mode model reference adaptive system (SM-MRAS) algorithm [8], extended Kalman filter (EKF) algorithm [9], and Luenberger Observer algorithm [10]. Among them, sensorless control methods based on SMOs [11, 12] have achieved significant success in industrial applications owing to their strong robustness, fast dynamic response, and simple structure. However, the frequent switching of control signals in SMC can cause chattering in the system output, which can be mitigated by designing appropriate switching functions (e.g., using a saturation function instead of a traditional sign function) [13]. At low speeds, the back-EMF signal is weak, which sometimes requires a combination with other control methods suitable for low speeds to achieve high-precision control across the entire speed range. Furthermore, SMO performance relies on the accuracy of the motor's mathematical model, which affects the observation precision.

Ref. [14] proposed an improved super-twisting sliding mode observer that effectively alleviated the chattering problem inherent in traditional SMOs. However, high-frequency filtering consistency, system complexity, and robustness at extremely low speeds require optimization. Ref. [15] effectively suppressed chattering and improved speed estimation accuracy through an improved adaptive super-twisting SMO (IAST-SMO) and super-twisting quadrature signal generator (ST-QSG). However, the system struggled to operate stably at very low speeds owing to the weak back-EMF. Ref. [16] proposed a high-order nonlinear super-twisting SMO (HNST-SMO) that employs an adaptive gain-based $f(x)$ function as the switching function, effectively solving the chattering problem caused by the sign function. Nevertheless, the accuracy of speed estimation still needs to be improved Ref. [17] proposed a low-chattering sensorless control strategy using a novel adaptive fast power reaching law sliding mode observer combined with an extended state observer-based high-order phase-locked loop, improving the system estimation accuracy and dynamic performance. However, its adaptability at extremely low speeds has not been explicitly addressed, and its adaptive regulation capability requires optimization. Ref. [18] proposed a robust sensorless control strategy using a full-order super-twisting sliding mode observer combined with a Harmonic-Resonant Feedforward Phase-Locked Loop (HRF-

* Corresponding author: Zhonggen Wang (zgwang@ahu.edu.cn).

PLL), achieving stable operation under lowspeed, zero-speed reversal, and sudden load change conditions. However, the resonant parameters of this control method need to match the harmonic frequencies, and its adaptability under extreme parameter perturbations has not been fully verified. Ref. [19] proposed a sensorless control strategy using a two-degree-of-freedom pre-filter and a Pre-filter-Embedded Adaptive Compensation PLL, decoupling the strong coupling between speed and position estimation and suppressing chattering. However, the strategy was sensitive to the stator inductance parameters, and the cutoff frequency of the pre-filter required a trade-off between the high-speed and low-speed performance. Ref. [20] designed an Adaptive Super-Twisting SMO and a Gain-Compensated Quasi-Resonant PLL to address issues in traditional schemes such as poor dynamic tracking, DC offset, and harmonic interference, but the parameter tuning process was complex. Ref. [21] replaced the discontinuous sign function with a continuous nonsmooth term and designed an Enhanced Quadrature PLL, effectively balancing the trade-off between anti-interference performance and phase delay. However, the low-speed adaptability requires further extension. Ref. [22] proposed a high-order PLL based on an Extended State Observer (ESO), considering the dynamic process, which improved the control accuracy of the PLL but had a limited compensation capability for nonlinear disturbances. Ref. [23] proposed a suppression strategy for estimated position errors based on a Full-Order Sliding Mode Observer (SMO) and a novel Phase-Locked Loop (PLL). This approach effectively cancels harmonic interference and phase delay generated during the back EMF estimation process of the Full-Order SMO, thereby reducing rotor position estimation errors across a wide range of speeds. Ref. [24] proposed an improved method combining a finite-control-set PLL and MRAS-based online inductance identification technique. This method abandons the PI controller, optimizes the cost function and iterative algorithm, and leverages the frequency offset resistance characteristic of the SMO, thereby resolving system stability issues. However, inductance cannot be identified when the active power is zero.

Therefore, to reduce the estimation errors of the rotor position and speed, this study integrates a novel adaptive super-twisting sliding mode observer and a high-gain phase-locked loop with a multimodal nonlinear function, which effectively enhances the system's robustness and estimation accuracy. Finally, the effectiveness of the proposed control strategy was verified through simulations and experiments.

2. MATHEMATICAL MODEL OF PMSM

In this study, the stator voltage equations of the PMSM in the stationary reference frame ($\alpha\beta$) can be expressed as:

$$\begin{bmatrix} u_\alpha \\ u_\beta \end{bmatrix} = \begin{bmatrix} R+pL_s & 0 \\ 0 & R+pL_s \end{bmatrix} \begin{bmatrix} i_\alpha \\ i_\beta \end{bmatrix} + \begin{bmatrix} e_\alpha \\ e_\beta \end{bmatrix} \quad (1)$$

where u_α and u_β represent the stator voltage; i_α and i_β represent the stator current,; e_α and e_β represent the back electromotive force on the α-axis and β-axis, respectively; R is the stator resistance; and L_s is the stator inductance.

According to Equation (1), the state-space equation of the stator current can be expressed as:

$$\frac{\mathrm{d}}{\mathrm{d}t}\begin{bmatrix} i_\alpha \\ i_\beta \end{bmatrix} = -\frac{R}{L_s}\begin{bmatrix} i_\alpha \\ i_\beta \end{bmatrix} + \frac{1}{L_s}\begin{bmatrix} u_\alpha \\ u_\beta \end{bmatrix} - \frac{1}{L_s}\begin{bmatrix} e_\alpha \\ e_\beta \end{bmatrix} \quad (2)$$

where the back electromotive force (back-EMF) can be expressed as:

$$\begin{bmatrix} e_\alpha \\ e_\beta \end{bmatrix} = \omega_e \psi_f \begin{bmatrix} -\sin\theta_e \\ \cos\theta_e \end{bmatrix} \quad (3)$$

where ω_e, ψ_f and θ_e represent the electrical angular velocity, permanent magnet flux linkage, and electrical angle, respectively.

From Equation (3), the back electromotive force contains all information regarding the rotor position and speed of the motor. Therefore, the rotor position and speed can be precisely calculated only by accurately obtaining the back-EMF.

3. SLIDING MODE OBSERVER

3.1. Traditional Sliding Mode Observer

To obtain the estimated back-EMF, the traditional SMO is designed as:

$$\frac{\mathrm{d}}{\mathrm{d}t}\begin{bmatrix} \hat{i}_\alpha \\ \hat{i}_\beta \end{bmatrix} = -\frac{R}{L_s}\begin{bmatrix} \hat{i}_\alpha \\ \hat{i}_\beta \end{bmatrix} + \frac{1}{L_s}\begin{bmatrix} u_\alpha \\ u_\beta \end{bmatrix} - \frac{1}{L_s}\begin{bmatrix} k*\mathrm{sign}(\tilde{i}_\alpha) \\ k*\mathrm{sign}(\tilde{i}_\beta) \end{bmatrix} \quad (4)$$

where $\hat{i}_\alpha$ and $\hat{i}_\beta$ denote the estimated stator currents.

Then, the sliding mode function is defined as:

$$\mathbf{s} = \begin{bmatrix} s_\alpha \\ s_\beta \end{bmatrix} = \begin{bmatrix} \tilde{i}_\alpha \\ \tilde{i}_\beta \end{bmatrix} = \begin{bmatrix} \hat{i}_\alpha - i_\alpha \\ \hat{i}_\beta - i_\beta \end{bmatrix} \quad (5)$$

where i_α and i_β denote the actual stator currents; s_α and s_β denote the stator current errors.

By subtracting Equation (2) from Equation (4), the state-space equation of the stator current error can be expressed as:

$$\frac{\mathrm{d}}{\mathrm{d}t}\begin{bmatrix} \tilde{i}_\alpha \\ \tilde{i}_\beta \end{bmatrix} = -\frac{R}{L_s}\begin{bmatrix} \tilde{i}_\alpha \\ \tilde{i}_\beta \end{bmatrix} + \frac{1}{L_s}\begin{bmatrix} e_\alpha \\ e_\beta \end{bmatrix} - \frac{1}{L_s}\begin{bmatrix} k*\mathrm{sign}(\tilde{i}_\alpha) \\ k*\mathrm{sign}(\tilde{i}_\beta) \end{bmatrix} \quad (6)$$

From Equation (6), it can be observed that when the system state approaches the sliding mode surface ($p\tilde{i}_\alpha = p\tilde{i}_\beta = \tilde{i}_\alpha = \tilde{i}_\beta = 0$), the back-EMF can be expressed as:

$$\begin{bmatrix} e_\alpha \\ e_\beta \end{bmatrix} = \begin{bmatrix} k^*\mathrm{sign}\,(\tilde{i}_\alpha) \\ k^*\mathrm{sign}\,(\tilde{i}_\beta) \end{bmatrix} \quad (7)$$

According to Equation (7), the control law employing the sign function exhibits discontinuity, and generally, a low-pass filter must be added:

$$\begin{cases} \frac{de_\alpha}{dt} = \frac{(-e_\alpha + k*\mathrm{sign}(\tilde{i}_\alpha))}{\tau} \\ \frac{de_\beta}{dt} = \frac{(-e_\beta + k*\mathrm{sign}(\tilde{i}_\beta))}{\tau} \end{cases} \quad (8)$$

A schematic of the traditional sliding mode observer is shown in Figure 1.

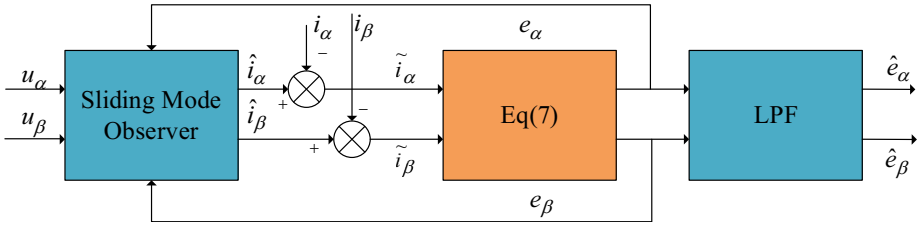

FIGURE 1. Block diagram of the traditional sliding mode observer.

3.2. Multimodal Nonlinear Function

The switching function in a traditional sliding mode observer employs a sign function. Although the sign function is simple in design and easy to implement, its discontinuity at the origin can lead to significant chattering in the sliding mode observer. To address this issue, this study proposes a multimodal nonlinear function, denoted as $f(x)$, to replace the sign function. Its expression is as follows:

$$f(x)=\begin{cases}1 & x\geq a\\ \ln(\frac{e-1}{a}x+1) & 0<x<a\\ -\ln(-\frac{e-1}{a}x+1) & -a<x<0\\ -1 & x\leq -a\end{cases} \tag{9}$$

The value of a is directly related to the chattering suppression effect and the control accuracy of the system. The corresponding functions $f(x)$ for different values of a are shown in Figure 2.

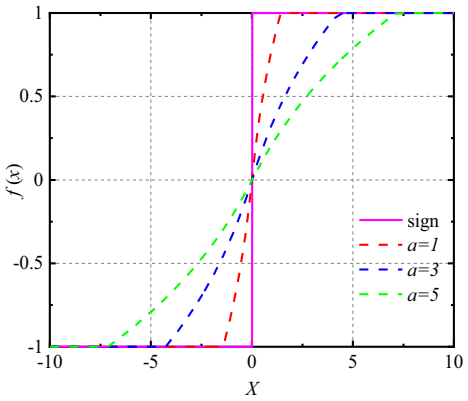

FIGURE 2. Switching function under different values of a.

3.3. Novel Adaptive Super-Twisting Algorithm

Traditional sliding mode observers employ a first-order constant-rate reaching law, which can lead to issues such as limited low-speed performance and a conflict between chattering suppression and reaching speed. In contrast, the super-twisting sliding mode observer utilizes a second-order super-twisting algorithm, offering advantages such as a higher observation accuracy and strong robustness.

The formula for the commonly used second-order super-twisting algorithm is as follows:

$$\begin{cases}\frac{dx_1}{dt}=-k_1\left|\bar{x}_1\right|^{0.5}\text{sign}(\bar{x}_1)+x_2\\ \frac{dx_2}{dt}=-k_2\text{sign}(\bar{x}_1)\end{cases} \tag{10}$$

where x_1 and x_2 are the estimated state variables; $\bar{x}_1=\hat{x}_1-x_1$ is the observation error; k_1 and k_2 are sliding mode parameters.

A novel adaptive nonlinear super-twisting algorithm is proposed to overcome the chattering phenomenon in traditional sliding mode observers. This method enhances convergence speed, adaptability, and low-speed observation performance by incorporating a nonlinear function and introducing an adaptive gain structure.

The formula of the novel adaptive nonlinear super-twisting algorithm is as follows:

$$\begin{cases}\frac{dx_1}{dt}=-k_1\frac{x_1}{\delta+9e^{-\lambda|x_1|}}f(x_1)-k_2\int x_1dx-k_3x_1+x_2\\ \frac{dx_2}{dt}=-k_4\frac{x_1}{\delta+9e^{-\lambda|x_1|}}f(x_1)\end{cases} \tag{11}$$

where k_i, δ, and λ are the adaptive observer gain parameters, and $k_i>0$, $\delta>0$, $\lambda>0$.

Among them, the parameter $-k_i\frac{x_1}{\delta+9e^{-\lambda|x_1|}}f(x_1)$ possesses dynamic adjustment capability, and $-k_2\int x_1dx-k_3x_1$ enhances the anti-interference capability and stability of the system. When the observation error $|x_1|$ is large (during motor startup or sudden speed changes), that is, $9e^{-\lambda|x_1|}\approx 0$, the denominator is approximately $\delta+9$, resulting in a larger gain that accelerates error convergence. When the observation error $|x_1|$ is small (during steady-state motor operation), that is, $9e^{-\lambda|x_1|}\approx 9$, the denominator is approximately $\delta+9$, leading to a reduced gain that better suppresses chattering. Gain k_4 exhibits better adaptability to control input x_2, enabling the system to adapt to different magnitudes of state errors and optimize the convergence characteristics.

3.4. Performance Analysis

Based on Equations (4), (9), and (11), the formula for the novel adaptive nonlinear super-twisting sliding mode observer (NANST-SMO) is derived as follows:

$$\frac{\mathrm{d}}{\mathrm{d}t}\begin{bmatrix}\hat{i}_\alpha\\ \hat{i}_\beta\end{bmatrix}=-\frac{R}{L_s}\begin{bmatrix}\hat{i}_\alpha\\ \hat{i}_\beta\end{bmatrix}+\frac{1}{L_s}\begin{bmatrix}u_\alpha\\ u_\beta\end{bmatrix}-\frac{1}{L_s}$$
$$\begin{bmatrix}k_1\frac{\overline{i_a}}{\delta+9e^{-\lambda|\overline{i_a}|}}f(\overline{i_a})+k_2\int\overline{i_a}+k_3\overline{i_a}+k_4\int\frac{\overline{i_a}}{\delta+9e^{-\lambda|\overline{i_a}|}}f(\overline{i_a})\\ k_1\frac{\overline{i_\beta}}{\delta+9e^{-\lambda|\overline{i_\beta}|}}f(\overline{i_\beta})+k_2\int\overline{i_\beta}+k_3\overline{i_\beta}+k_4\int\frac{\overline{i_\beta}}{\delta+9e^{-\lambda|\overline{i_\beta}|}}f(\overline{i_\beta})\end{bmatrix} \tag{12}$$

The structural block diagram of the NANST-SMO is shown in Figure 3.

To validate the feasibility of NANST-SMO, the simulation rotational speed is set to $300\,\mathrm{r}\cdot\mathrm{min}^{-1}$. The performances of

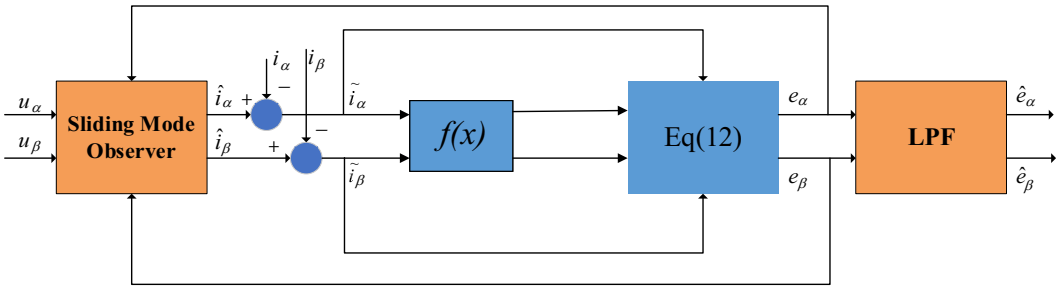

FIGURE 3. Block diagram of the NANST-SMO structure.

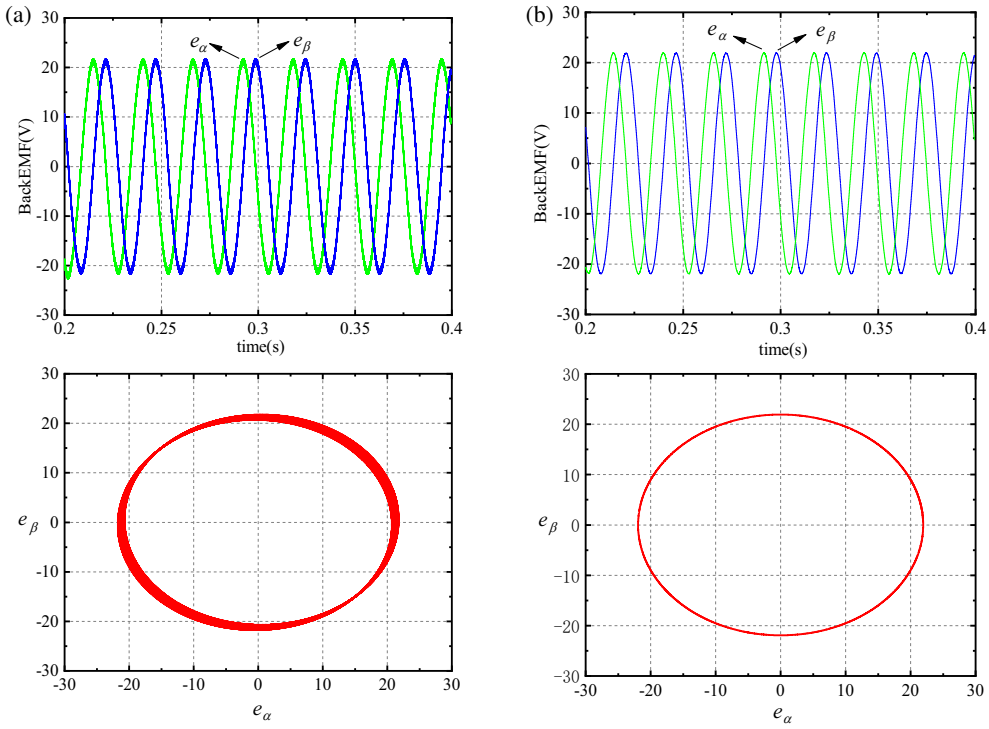

FIGURE 4. Back-EMF waveforms. (a) RSMO. (b) NANST-SMO.

both the Referenced MSO (RSMO) and NANST-SMO schemes were compared, and the results are shown in Figure 4. Figure 4(a) presents the back-EMF waveform and the Lissajous figure for RSMO, whereas Figure 4(b) presents those for NANST-SMO. As shown in Figure 4, the contour of the Lissajous figure for RSMO is relatively coarse, indicating high-frequency chattering in the rotor position observation. The Lissajous figure for NANST-SMO is smoother and tends toward a circle, demonstrating that high-frequency noise and chattering in the rotor position observation signal are effectively suppressed. This verified the stability of the NANST-SMO scheme.

3.5. Stability Analysis

To demonstrate the stability of the NANST-SMO-based system, the Lyapunov stability theorem is adopted, and the following Lyapunov function is constructed:

$$V = \frac{1}{2}(i_\alpha^2 + i_\beta^2) \tag{13}$$

Differentiating V with respect to time yields:

$$\dot{V} = i_\alpha \dot{i}_\alpha + i_\beta \dot{i}_\beta \tag{14}$$

Substituting Equation (12) into the above expression yields:

$$\begin{aligned} \dot{V} &= i_\alpha \left(\frac{R}{L_S} i_\alpha + \frac{1}{L_S} u_\alpha - \frac{1}{L_S} M_\alpha \right) \\ &\quad + i_\beta \left(\frac{R}{L_S} i_\beta + \frac{1}{L_S} u_\beta - \frac{1}{L_S} M_\beta \right) \end{aligned} \tag{15}$$

where:

$$\begin{aligned} M_\alpha &= k_1 \frac{\overline{i_a}}{\delta + 9e^{-\lambda|\overline{i_a}|}} f(\overline{i_a}) + k_2 \int \overline{i_a} \\ &\quad + k_3 \overline{i_a} + k_4 \int \frac{\overline{i_a}}{\delta + 9e^{-\lambda|\overline{i_a}|}} f(\overline{i_a}) \end{aligned} \tag{16}$$

$$M_\beta = k_1 \frac{\overline{i_\beta}}{\delta + 9e^{-\lambda|\overline{i_\beta}|}} f(\overline{i_\beta}) + k_2 \int \overline{i_\beta}$$

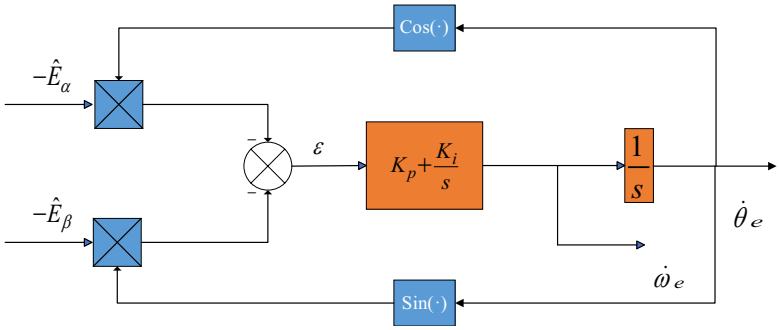

FIGURE 5. Conventional phase-locked loop (PLL).

$$+k_3\overline{i_\beta}+k_4\int\frac{\overline{i_\beta}}{\delta+9e^{-\lambda|\overline{i_\beta}|}}f(\overline{i_\beta}) \tag{17}$$

After simplification, we obtain:

$$\begin{aligned}\dot{V}&=-\frac{R}{L_s}(i_\alpha^2+i_\beta^2)+\frac{1}{L_s}(i_\alpha u_\alpha+i_\beta u_\beta)-\frac{1}{L_s}(i_\alpha M_\alpha+i_\beta M_\beta)\\&=-\frac{R}{L_s}(i_\alpha^2+i_\beta^2)-\frac{i_\alpha}{L_s}(M_\alpha-u_\alpha)-\frac{i_\beta}{L_s}(M_\beta-u_\beta)\end{aligned} \tag{18}$$

Because the nonlinear terms M_α and M_β include functions similar to $f(x)$, and the $f(x)$ function is bounded and smooth, while the values of i_α, i_β, u_α, u_β are limited in range, the compensation terms include $k_2\int x_1dx$ and k_3x_1 individually, and the parameter k_i can take a relatively wide range of values, which ensures that M_α and M_β possess high adaptability, thereby guaranteeing $\dot{V}\leq 0$. Therefore, the system is globally asymptotically stable.

4. PHASE-LOCKED LOOP

4.1. Traditional Phase-Locked Loop (PLL)

When the system state point moves near the sliding mode surface, high-frequency chattering is generated. The estimation method based on the arctangent function will also introduce chattering into the division operation, thereby causing a large rotor position estimation error. The schematic diagram of the conventional phase-locked loop (PLL) is shown in Figure 5.

The expression of the rotor position error signal is given as follows:

$$\begin{aligned}\varepsilon&=-\hat{E}_\alpha\cos\hat{\theta}_e-\hat{E}_\beta\sin\hat{\theta}_e\\&=\phi\sin\theta_e\cos\hat{\theta}_e-\phi\cos\theta_e\sin\hat{\theta}_e\\&=\phi\sin(\theta_e-\hat{\theta}_e)\approx\phi(\theta_e-\hat{\theta}_e)\end{aligned} \tag{19}$$

where $\phi=\hat{\omega}_e\psi_f$ denotes the estimated back-EMF amplitude, and $\hat{\omega}_e$ denotes the estimated electrical angular velocity.

The transfer function of the Phase-Locked Loop (PLL) is given as follows:

$$G(s)=\frac{\hat{\theta}_e}{\theta_e}=\frac{2\xi\omega_n s+\omega_n^2}{s^2+2\xi\omega_n s+\omega_n^2} \tag{20}$$

where $\xi=\sqrt{\phi K_i}$, $\omega_n=\frac{K_p}{2}\sqrt{\frac{\phi}{K_i}}$. K_p and K_i denote the proportional gains and integral gains of proportional-integral (PI) controller, respectively.

4.2. High-Order Gain Compensation Phase-Locked Loop (HGC-PLL)

The Extended State Observer (ESO), due to its advantages such as flexible parameter tuning and strong compatibility, is widely applied in the sensorless control of PMSM. The structural formula of the ESO designed for a Higher-Order Phase-Locked Loop (HPLL) is as follows:

$$\begin{cases}\varepsilon=y_1-\theta_e\\\dot{y}_1=y_2-\beta_1 f(\varepsilon)-\beta_2\int f(\varepsilon)\\\dot{y}_2=y_3-\beta_3 f(\varepsilon)\\\dot{y}_3=-\beta_4\ln(5|\varepsilon|+1)f(\varepsilon)\end{cases} \tag{21}$$

4.3. Compensation Strategy

In this context, the closed-loop speed is the speed filtered by a Low-Pass Filter, whereas the speed used in SMO is an unfiltered version. Consequently, there is inevitably a deviation between the estimated rotor position and actual rotor position, denoted as:

$$\Delta\eta_{\text{error}}=\int\hat{\omega}_p\,\mathrm{d}t-\int\hat{\omega}_e\,\mathrm{d}t \tag{22}$$

Rotor position is:

$$\hat{\theta}_e=\hat{\theta}_{SMO}+\Delta\eta_{\text{error}} \tag{23}$$

where $\hat{\theta}_{SMO}$ represents the rotor position output by the HGC-PLL.

Finally, the circuit schematic diagram of the final higher-order gain compensation phase-locked loop (HGC-PLL) is shown in Figure 6.

4.4. Proof of Stability

Define the state variables as:

$$\begin{cases}x_1=\varepsilon\\x_2=y_2\\x_3=y_3\end{cases} \tag{24}$$

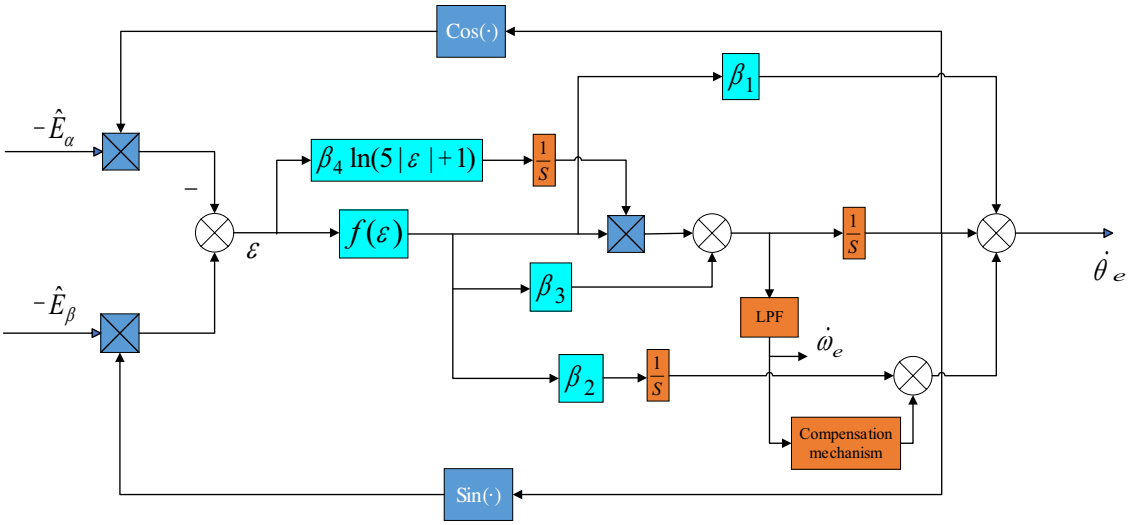

FIGURE 6. Circuit schematic diagram of HGC-PLL.

From Equation (21), it can be derived that:

$$\begin{cases} \dot{x}_1 = x_2 - \beta_1 f(x_1) - \beta_2 \int f(x_1) \\ \dot{x}_2 = x_3 - \beta_3 f(x_1) \\ \dot{x}_3 = -\beta_4 \ln(5|\varepsilon| + 1) f(x_1) \end{cases} \tag{25}$$

Lyapunov function is:

$$V(x) = \frac{1}{2}x_1^2 + \frac{1}{2}x_2^2 + \frac{1}{2}x_3^2 \tag{26}$$

Taking the derivative of V yields:

$$\dot{V} = x_1\dot{x}_1 + x_2\dot{x}_2 + x_3\dot{x}_3 \tag{27}$$

Substituting Equation (28) gives:

$$\begin{aligned} \dot{V} &= x_1(x_2 - \beta_1 f(x_1) - \beta_2 \int f(x_1)) + x_2(x_3 - \beta_3 f(x_1)) \\ &\quad + x_3(-\beta_4 \ln(5|\varepsilon| + 1) f(x_1)) \\ &= x_1x_2 + x_2x_3 - \beta_1 x_1 f(x_1) - x_1\beta_2 \int f(x_1) \\ &\quad - \beta_3 x_2 f(x_1) - \beta_4 x_3 \ln(5|\varepsilon| + 1) f(x_1) \end{aligned} \tag{28}$$

From Equation (9), it can be observed that $x_1 f(x_1) \geq 0$, magnitudes of $\beta_1 x_1 f(x_1)$ and $x_1\beta_2 \int f(x_1)$ are related to gains β_1 and β_2. Additionally, parameters β_1 and β_2 exist independently, offering considerable flexibility in their selection. Considering that the domain of variable $f(x_1)$ is constrained to a specific interval, that is, $|f(x_1)| \leq 1$, consequently, the terms $\beta_3 x_2 f(x_1)$ and $\beta_4 x_3 \ln(5|\varepsilon|+1) f(x_1)$ effectively avoid signal discretization distortion. By appropriately selecting the values of $\beta_1, \beta_2, \beta_3, \beta_4$, the cross terms involving x_1x_2 and x_2x_3 can be prevented from significantly affecting the stability.

Therefore, under appropriate selection, that is, $\beta_1 > 0, \beta_2 > 0, \beta_3 > 0, \beta_4 > 0$, which ensures $\dot{V} \leq 0$, by appropriately selecting x, the system becomes globally asymptotically stable.

5. SIMULATION ANALYSIS

To verify the feasibility of combining NANSTSMO and HGC-PLL as proposed in this paper, three schemes are presented for comparison: Scheme 1 combines a Traditional Sliding Mode Observer and a Phase-Locked Loop (TSMO-PLL); Scheme 2 combines an RSMO and a PLL (RSMO-PLL) [25]; and Scheme 3 combines the proposed NANSTSMO with HGCPLL (NANSTSMO-HGCPLL).

Based on the permanent magnet synchronous motor (PMSM) control block diagram illustrated in Figure 7, simulations were performed in MATLAB/Simulink. The current and speed loops were controlled using conventional PI regulators, and the sampling period was fixed at 10 µs.

5.1. No-Load Speed Analysis

With a rotational speed set to 300 r · min^{-1}, Figures 8, 9, and 10 show the rotational speed waveforms for TSMO-PLL, RSMO-PLL, and NANSTSMO-HGCPLL, respectively.

As shown in Figure 8, Scheme 1 exhibits significant oscillation during the initial stages. In the overshoot phase, the speed error range of the PMSM is $-200 \sim 180$ r · min^{-1}. In the steady-state phase, the speed error is $-35 \sim 30$ r · min^{-1}, corresponding to a maximum speed error of 65 r · min^{-1}. As shown in Figure 9, Scheme 2 exhibits a significant speed overshoot during the initial stage. In the overshoot phase, the speed error range of the PMSM is $-41 \sim 260$ r · min^{-1}. In the steady-state phase, the speed error is $-2 \sim -0.6$ r · min^{-1}, corresponding to a maximum speed error of -1.4 r · min^{-1}. As shown in Figure 10, Scheme 3 exhibits a relatively minor speed overshoot during the initial stage. In the overshoot phase, the speed error range of the PMSM is $-43 \sim 104$ r · min^{-1}. In the steady-state phase, the speed error is $-0.2 \sim 0.2$ r · min^{-1}, corresponding to a maximum speed error of 0.4 r · min^{-1}.

In summary, Scheme 3 suppresses chattering more effectively, exhibits the smallest steady-state error, and demonstrates the best overall performance.

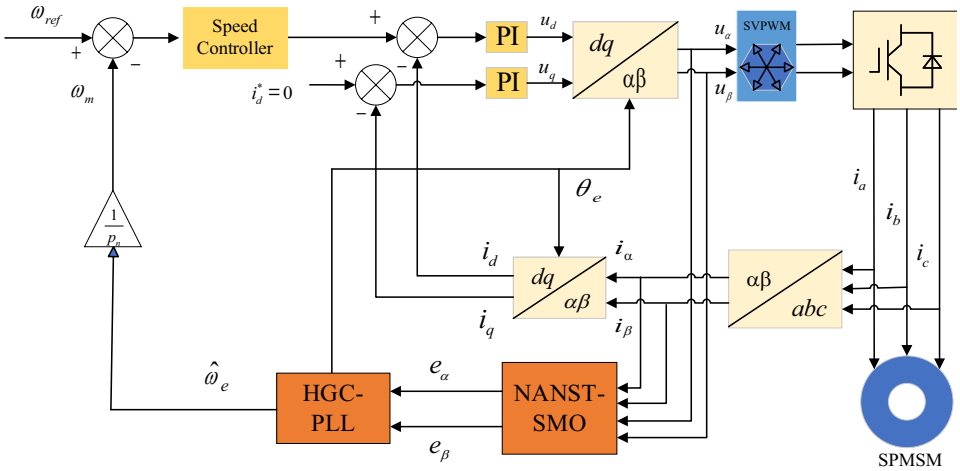

FIGURE 7. Control block diagram of the PMSM system.

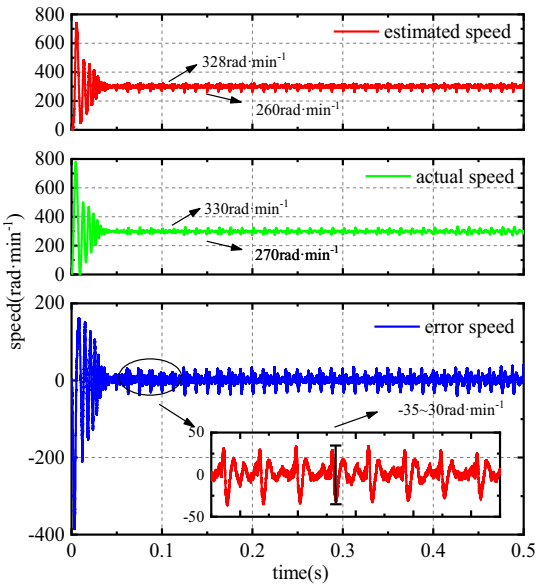

FIGURE 8. Waveforms of speed and speed error under no-load condition for TSMO-PLL.

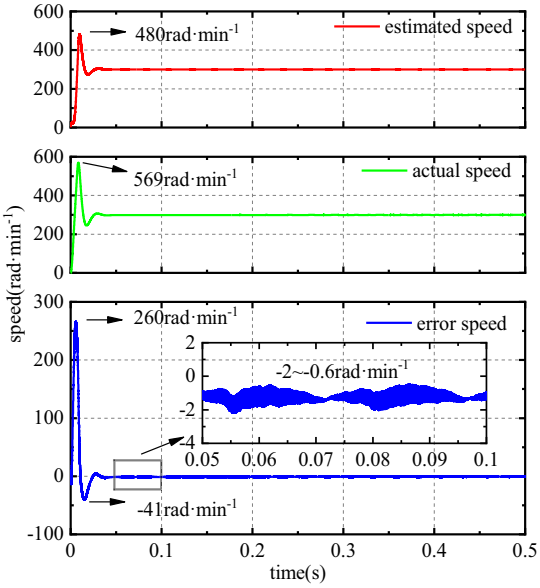

FIGURE 9. Waveforms of speed and speed error under no-load condition for RSMO-PLL.

5.2. Rotor Position Analysis

Figures 11, 12, and 13 show the rotor position waveforms and rotor position error waveforms under no-load speed conditions.

From Figure 11, in Scheme 1, the rotor position error during the initial simulation stage was approximately 0.45 rad, reducing to approximately 0.2 rad at steady state, respectively. When the same rotor position was reached, the time difference between the estimated rotor position and actual rotor position was 0.0025 s. From Figure 12, in Scheme 2, the rotor position error during the initial simulation stage was about 0.3 rad, reducing to approximately 0.13 rad at steady state. The time difference between the estimated and actual rotor positions at the same rotor position was 0.002 s. From Figure 13, in Scheme 3, the rotor position error during the initial stage was only about 0.01 rad and further decreases to approximately 0.0004 rad at the steady state. The time difference between the estimated and actual rotor positions for the same rotor position was 0.0001 s.

The simulation results indicate that the control method of the NANSTSMO-HGCPLL achieves a higher position tracking accuracy and better control performance.

5.3. Current Error Analysis

Figure 14 shows the error current waveforms under three different control strategies ($\tilde{i}_\alpha = \hat{i}_\alpha - i_\alpha$). As shown in Figure 15, the error current ranges for Schemes 1, 2, and 3 are $-0.25 \sim 0.25$ A, $-0.15 \sim 0.15$ A, and $-0.015 \sim 0.015$ A, respectively. This corresponded to peak-to-peak error currents of 0.5 A, 0.3 A, and 0.03 A.

The simulation results indicate that the error current curve of Scheme 3 is the smoothest and exhibits the lowest fluctuation frequency. This demonstrates that the current loop in Scheme 3 achieves better stability, directly reflecting its significant advantages in current control accuracy and system stability for the sensorless PMSM control system.

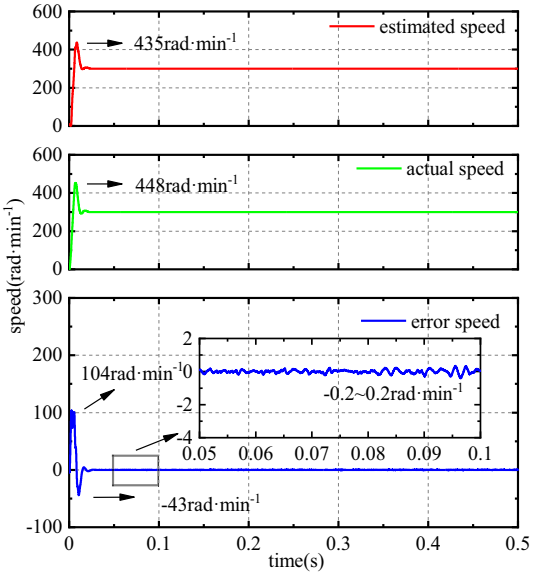

FIGURE 10. Waveforms of speed and speed error under no-load condition for NANSTSMO-HGCPLL.

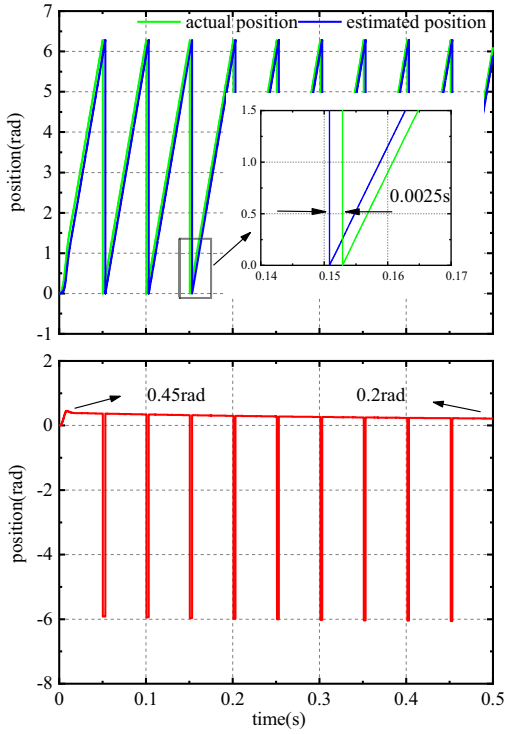

FIGURE 11. Waveforms of rotor position and position error under no-load condition for TSMO-PLL.

5.4. Loaded Speed Analysis

The rotational speed was set to 300 r · min^{-1}, and a sudden load increase of 10 N · m was applied when the simulation reaches 0.2 s. Figures 15, 16, and 17 show the speed waveforms under a sudden load increase for the three schemes.

From Figure 15, the estimated speed and actual speed decreased by 55 r · min^{-1} and 65 r · min^{-1}, respectively. The speed error varied within a range of $-30 \sim 35$ r · min^{-1}, and the maximum speed error is 65 r · min^{-1}. From Figure 16, the estimated speed and the actual speed decreased by 48 r · min^{-1}

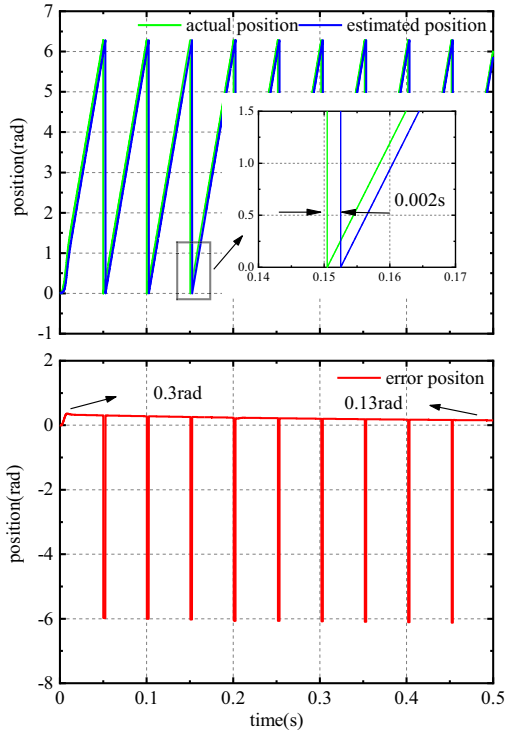

FIGURE 12. Waveforms of rotor position and position error under no-load condition for RSMO-PLL.

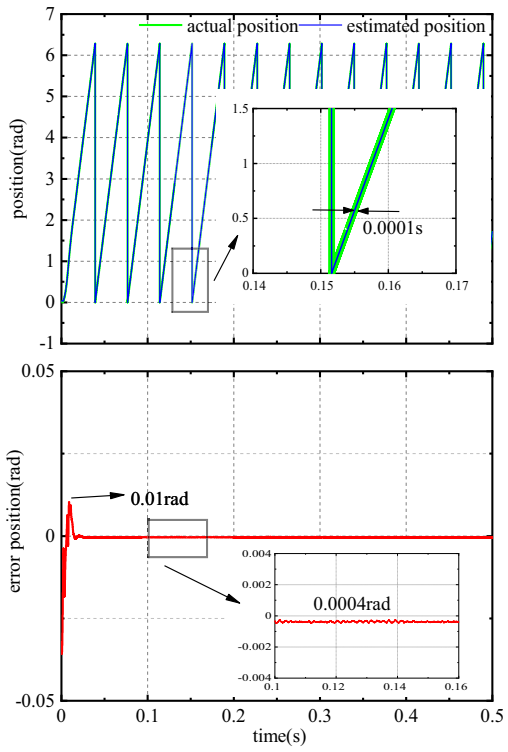

FIGURE 13. Waveforms of rotor position and position error under no-load condition for NANSTSMO-HGCPLL.

and 65 r · min^{-1}, respectively. The speed error varies within a range of $-34 \sim 20$ r · min^{-1}, corresponding to a peak speed error of 54 r · min^{-1}. From Figure 17, the estimated speed and actual speed decreased by 45 r · min^{-1} and 50 r · min^{-1}, respectively. The speed error varied within the range of $-20 \sim 14$ r · min^{-1}, leading to a peak speed error of 34 r · min^{-1}.

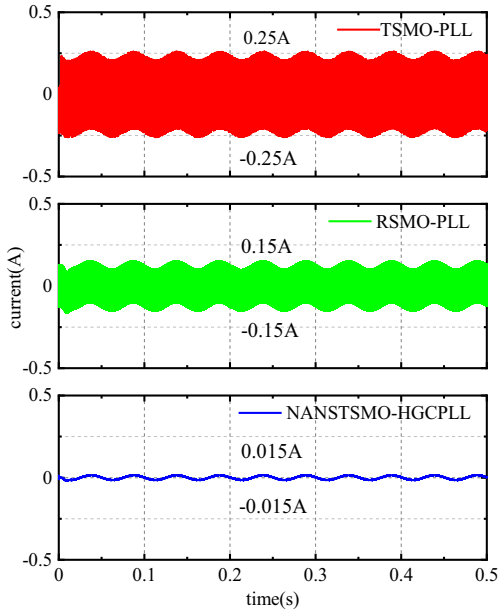

FIGURE 14. Error current.

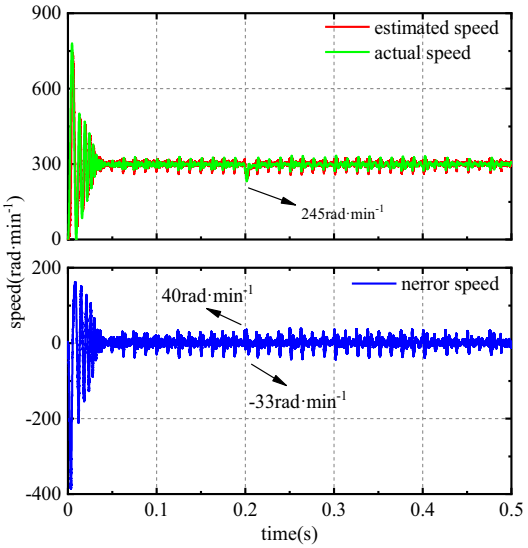

FIGURE 15. Speed waveforms under a sudden load increase for TSMO-PLL.

This demonstrates that the control strategy of the NANSTSMO-HGCPLL reduces the chattering caused by speed variations and improves the dynamic performance.

5.5. Variable-Speed Simulation

The speed was set to vary from $600\,\mathrm{r\cdot min^{-1}}$ to $900\,\mathrm{r\cdot min^{-1}}$, Figures 18, 19, and 20 present the variable-speed waveforms of the three control strategies: TSMO-PLL, RSMO-PLL, and NANSTSMO-HGCPLL, respectively.

From Figure 18, at the beginning of the speed change, the speed error varied from $-150\,\mathrm{r\cdot min^{-1}}$ to $161\,\mathrm{r\cdot min^{-1}}$. After the simulation was stabilized, the speed error lies between $-27\,\mathrm{r\cdot min^{-1}}$ and $25\,\mathrm{r\cdot min^{-1}}$, corresponding to an overall speed error of $52\,\mathrm{r\cdot min^{-1}}$. From Figure 19, at the beginning of the speed change, the speed error varies from $-50\,\mathrm{r\cdot min^{-1}}$ to $107\,\mathrm{r\cdot min^{-1}}$. After the simulation was stabilized, the speed error fell within $-2\,\mathrm{r\cdot min^{-1}}$ to $0\,\mathrm{r\cdot min^{-1}}$, corresponding to an overall speed error of $2\,\mathrm{r\cdot min^{-1}}$. From Figure 20, at the beginning of the speed change, the speed error varied from -34 r/min to 86 r/min. After the simulation was stabilized, the speed error falls within $-0.1\,\mathrm{r\cdot min^{-1}}$ to $0.1\,\mathrm{r\cdot min^{-1}}$, corresponding to an overall speed error of $0.2\,\mathrm{r\cdot min^{-1}}$.

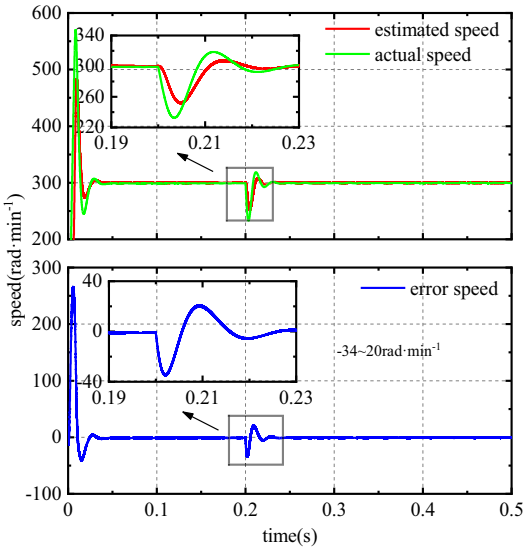

FIGURE 16. Speed waveforms under a sudden load increase for RSMO-PLL.

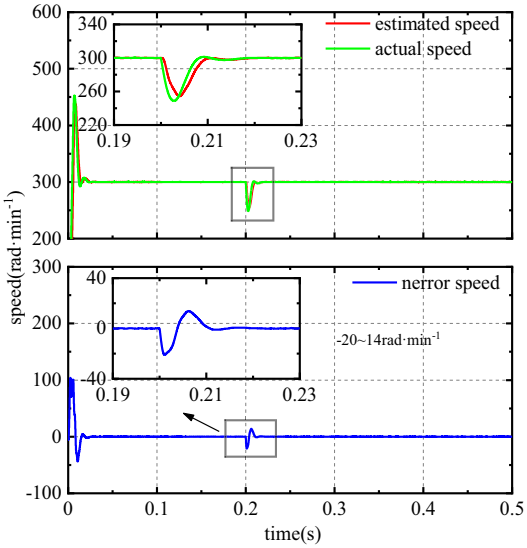

FIGURE 17. Speed waveforms under a sudden load increase for NANSTSMO-HGCPLL.

This demonstrates that the NANSTSMO-HGCPLL can effectively reduce the chattering induced by speed variations and improve the dynamic performance.

6. EXPERIMENTAL TEST ANALYSIS

To validate the effectiveness of the proposed method further, a control experiment was conducted on the motor test platform, as illustrated in Figure 21. The hardware system primarily consists of a permanent magnet synchronous motor

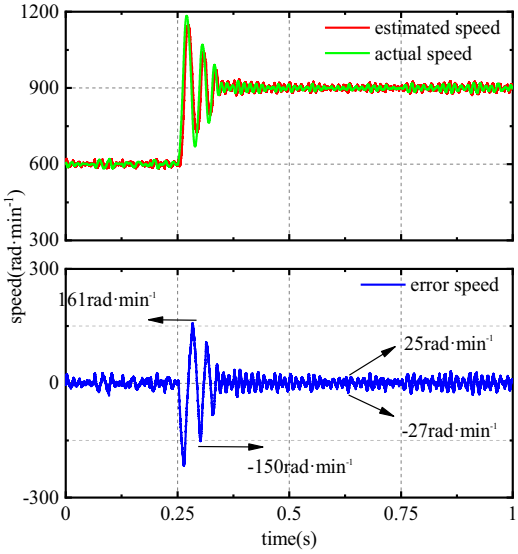

FIGURE 18. Variable-speed waveforms for TSMO-PLL.

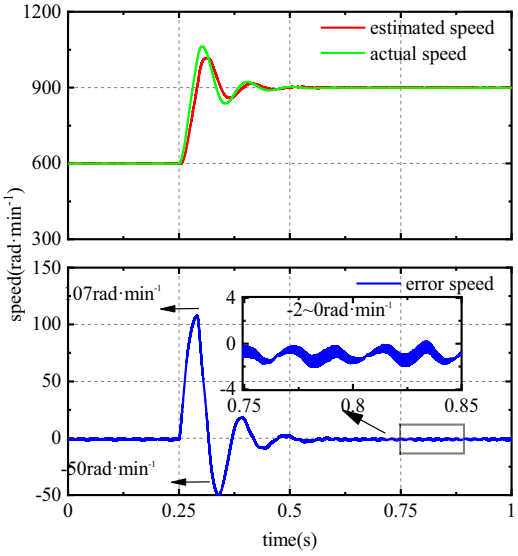

FIGURE 19. Variable-speed waveforms for RSMO-PLL.

(PMSM), a brushed DC motor, and a torque-speed sensor. The drive section was implemented based on a motor driver board and a digital signal processing (DSP) controller (model: TMS320F28335). The core component of the drive is an IRS2103STRPBF, which comprises six driver chips and twelve MOS transistors, enabling the simultaneous driving of the two motors.

The simulation parameters of the PMSM are listed in Table 1.

6.1. Unloaded Test

With the rotational speed set to $300\,\mathrm{r\cdot min^{-1}}$ and the experiment duration set to 5 s, a comparison of the speed waveforms for the TSMO-PLL, RSMO-PLL, and NANSTSMO-HGCPLL strategies, obtained under no-load conditions, is provided in Figures 22, 23, and 24. As shown in Figures 22, 23, and 24, under the control strategies of TSMO-PLL, RSMO-PLL, and NANSTSMO-HGCPLL, the estimated speeds were

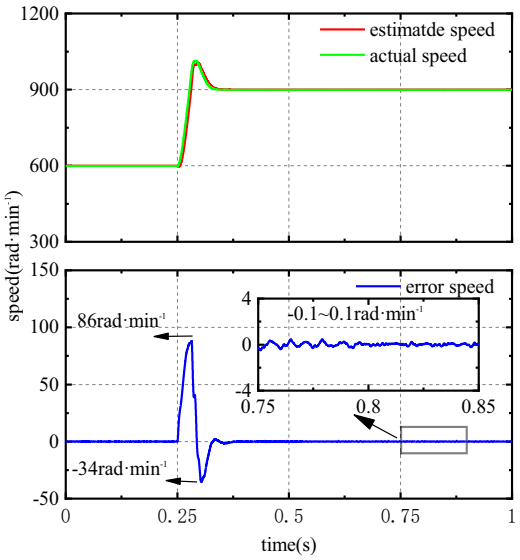

FIGURE 20. Variable-speed waveforms for NANSTSMO-HGCPLL.

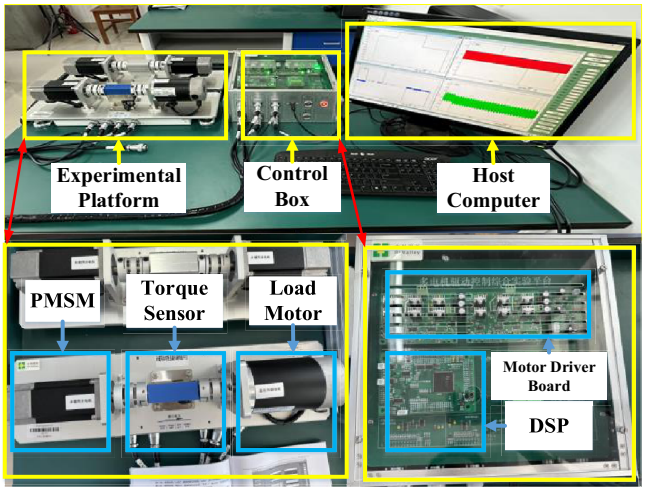

FIGURE 21. Motor test platform.

TABLE 1. Motor operating parameters.

Parameters	Values	Notes
P_n	4	Number of Pole Pairs
R_s	2.875 Ω	Stator Resistance
L_s	8.5 mH	Stator Inductance
J	$0.003\,\mathrm{kg\cdot m^2}$	Moment of Inertia
B	$0.008\,\mathrm{M\cdot m\cdot s}$	Damping Coefficient
ψ_f	0.175 Wb	Magnetic linkage
U_{dc}	311 V	DC voltage
P	400 W	Rated out power
N	$3000\,\mathrm{r\cdot min^{-1}}$	Rated speed
T	$1.27\,\mathrm{N\cdot m}$	Rated torque
I	12.5 A	Rated current

287 ∼ $312\,\mathrm{r\cdot min^{-1}}$, 294 ∼ $316\,\mathrm{r\cdot min^{-1}}$, and 301 ∼ $311\,\mathrm{r\cdot min^{-1}}$, respectively, with corresponding speed errors of -18 ∼ $14\,\mathrm{r\cdot min^{-1}}$, -6 ∼ $15\,\mathrm{r\cdot min^{-1}}$, and -2 ∼ $13\,\mathrm{r\cdot min^{-1}}$. The maximum errors for each strategy were $32\,\mathrm{r\cdot min^{-1}}$, $21\,\mathrm{r\cdot min^{-1}}$, and $15\,\mathrm{r\cdot min^{-1}}$.

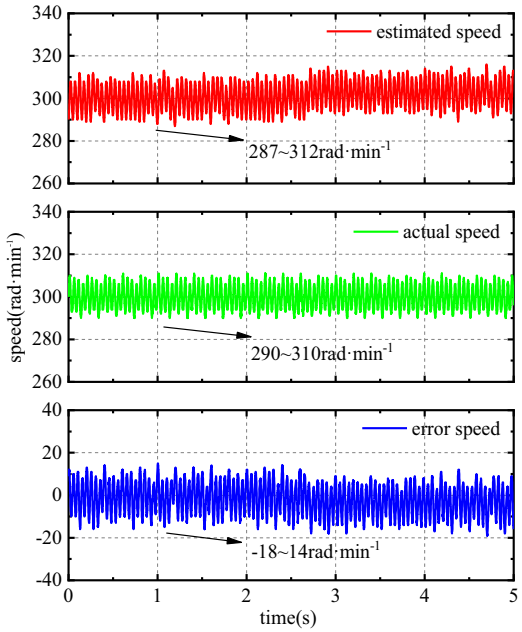

FIGURE 22. Speed waveforms under no-load conditions for TSMO-PLL.

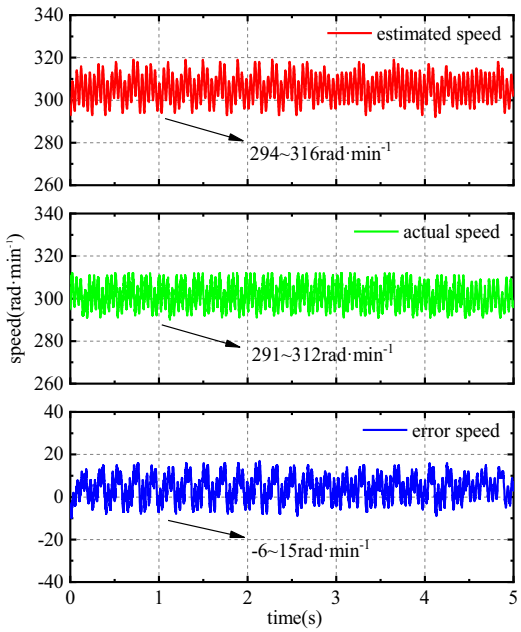

FIGURE 23. Speed waveforms under no-load conditions for RSMO-PLL.

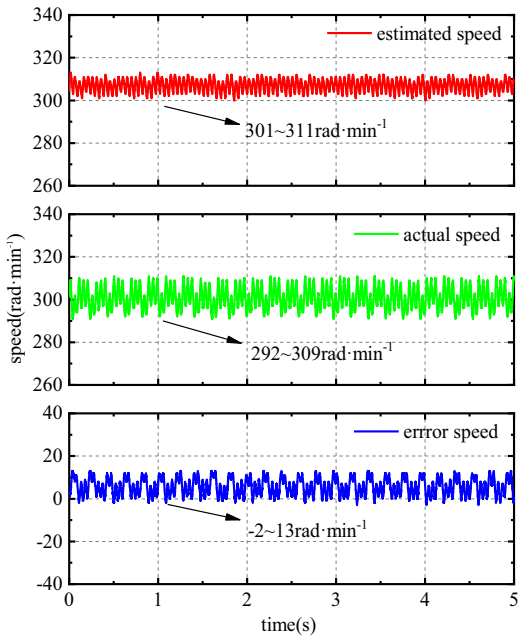

FIGURE 24. Speed waveforms under no-load conditions for NANSTSMO-HGCPLL.

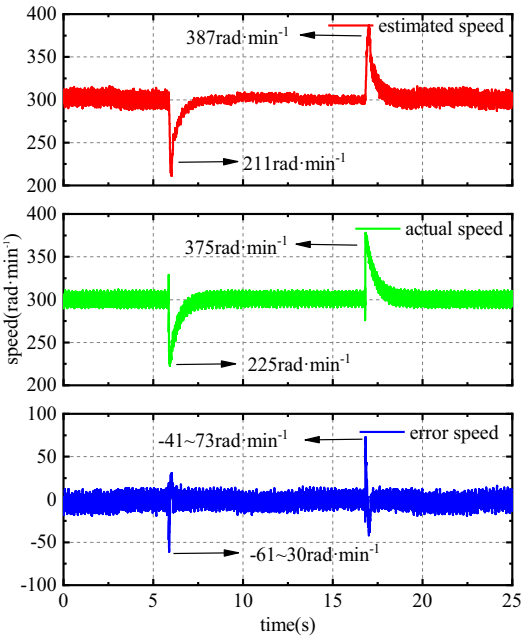

FIGURE 25. Speed waveforms under sudden load change conditions for TSMO-PLL.

These results demonstrate the superior chattering suppression effect and enhanced speed stability of the NANSTSMO-HGCPLL strategy.

6.2. Loading/Unloading Test Analysis

Experiments were conducted based on the no-load speed, and the experiment duration was set to 25 s. The load was applied and removed at the 6 s and 17 s marks, respectively.

Figures 25, 26, and 27 show the speed waveforms of the three schemes under these sudden load change conditions. As shown in Figures 25, 26, and 27, when the load was suddenly increased, the speed drop of Scheme 1 was $89\,\mathrm{r\cdot min^{-1}}$, and the speed error varies between $-61\,\mathrm{r\cdot min^{-1}}$ and $30\,\mathrm{r\cdot min^{-1}}$. In Scheme 2, the speed drop is $62\,\mathrm{r\cdot min^{-1}}$, with the speed error ranging from $-19\,\mathrm{r\cdot min^{-1}}$ to $39\,\mathrm{r\cdot min^{-1}}$. In Scheme 3, the speed drop was $41\,\mathrm{r\cdot min^{-1}}$, and the speed error lies between $-13\,\mathrm{r\cdot min^{-1}}$ and $34\,\mathrm{r\cdot min^{-1}}$. When the load was suddenly reduced, the estimated speed increases for the three control schemes were $87\,\mathrm{r\cdot min^{-1}}$, $67\,\mathrm{r\cdot min^{-1}}$, and $41\,\mathrm{r\cdot min^{-1}}$, respectively, with corresponding speed errors of $-41 \sim 73\,\mathrm{r\cdot min^{-1}}$, $-26 \sim 33\,\mathrm{r\cdot min^{-1}}$, and $-18 \sim 19\,\mathrm{r\cdot min^{-1}}$.

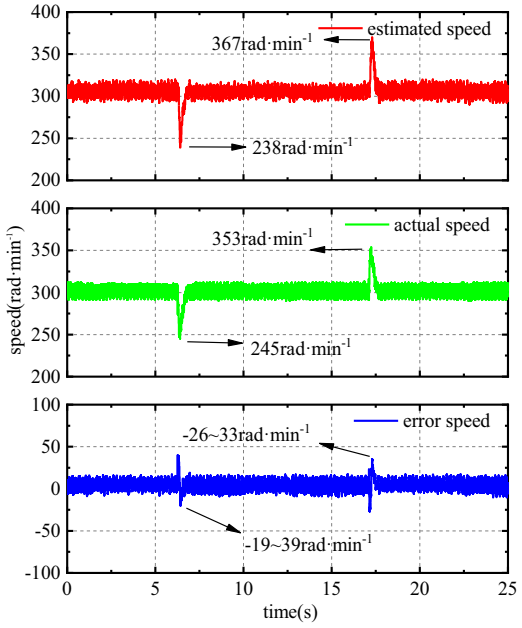

FIGURE 26. Speed waveforms under sudden load change conditions for RSMO-PLL.

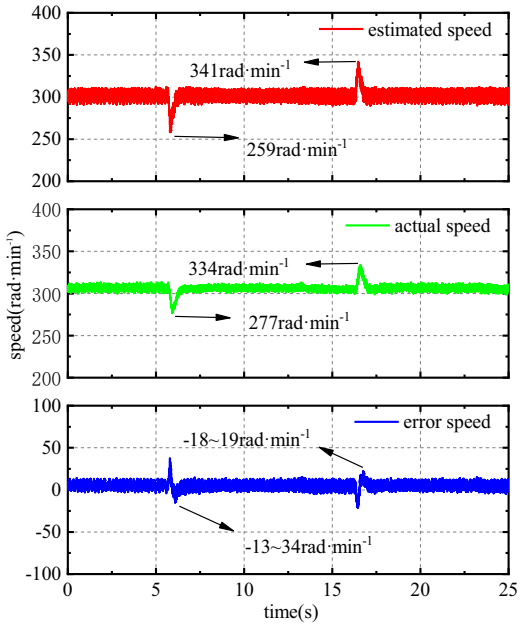

FIGURE 27. Speed waveforms under sudden load change conditions for NANSTSMO-HGCPLL.

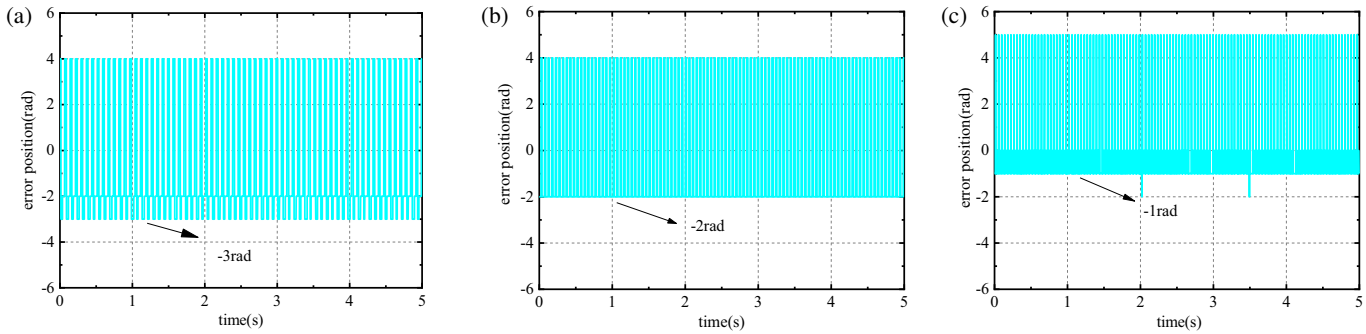

FIGURE 28. Rotor position error diagram. (a) TSMO-PLL. (b) RSMO-PLL. (c) NANSTSMO-HGCPLL.

It can be concluded that the NANSTSMO-HGCPLL control strategy exhibits the strongest load disturbance rejection capability, enabling better maintenance of the rotational speed stability.

6.3. Experimental Analysis of Rotor Position Error

Figure 28 shows the rotor position error waveforms for the three schemes. From Figures 28(a), (b), and (c), Scheme 1 is approximately -3 rad, Scheme 2 approximately -2 rad, and Scheme 3 approximately -1 rad. From this, it can be concluded that Scheme 1 exhibits significant chattering and errors. Scheme 2 reduces chattering through the RSMO, while Scheme 3, by enhancing NANSTSMO with the HGCPLL, transient response and steady-state accuracy are further improved, resulting in the smallest rotor position error. This demonstrates that compared to Schemes 1 and 2, Scheme 3 achieves more accurate position observation, smaller torque ripple, and better dynamic stability performance.

7. CONCLUSION

In this study, a control method based on a novel adaptive nonlinear super-twisting sliding mode observer (NANSTSMO) and high-order gain-compensated phase-locked loop (HGC-PLL) is proposed. The main results fall into the following categories:

1) A novel adaptive super-twisting sliding mode observer was designed, to enhance the dynamic response of the sliding mode observer.

2) A higher-order gain compensation phase-locked loop is proposed, which enhances the steady-state tracking accuracy of the rotor position and provides a stronger anti-interference capability.

3) A multimodal nonlinear function is designed to replace the sign function and is incorporated into both the NANSTSMO and HGCPLL, effectively suppressing chattering and enhancing control smoothness.

4) The NANSTSMO involves multiple adaptive gain parameters (k_i, δ, λ), while the HGCPLL requires the tuning of

gain coefficients (β_1, β_2, β_3, β_4) and parameters of the multimodal nonlinear function (a). The mutual coupling among these parameters increases the complexity of the tuning process, and iterative adjustment is required based on specific motor specifications and operating conditions. The solution is addressed by implementing fuzzy control. The core of this method lies in the coordination of parameters, which is achieved by adjusting the fuzzy rule base, the parameters of the membership functions, and the relevant defuzzification parameters, thereby optimizing the performance of the control system.

REFERENCES

[1] Kumar, S. and B. Singh, "Control of solar photovoltaic integrated sensorless PMSM driven three-wheeler electric vehicle," *IEEE Transactions on Industry Applications*, Vol. 61, No. 3, 4128–4138, 2025.

[2] Peng, Y., F. Chen, F. Chen, C. Wu, Q. Wang, Z. He, and S. Lu, "Energy-efficient train control: A comparative study based on permanent magnet synchronous motor and induction motor," *IEEE Transactions on Vehicular Technology*, Vol. 73, No. 11, 16 148–16 159, 2024.

[3] Yang, Z., T. Shen, X. Sun, H. Xu, and W. Pan, "Model predictive control of robot flexible joint motor based on lyapunov prediction model," *IEEE Transactions on Power Electronics*, Vol. 40, No. 8, 10 783–10 792, 2025.

[4] Wang, X., D. Luo, and D. Xiao, "Limit cycle analyses of extended EMF-based position-sensorless in IPMSM drives," *IEEE Transactions on Power Electronics*, Vol. 40, No. 5, 6519–6528, 2025.

[5] Dong, S., M. Zhou, C. Wang, and X. You, "A sensorless control method with identification of stator inductance for IPMSM at low-speed under low switching frequency," *IEEE Transactions on Transportation Electrification*, Vol. 10, No. 3, 5344–5354, 2024.

[6] Wu, S., C. Hu, Z. Zhao, and Y. Zhu, "High-accuracy sensorless control of permanent magnet linear synchronous motors for variable speed trajectories," *IEEE Transactions on Industrial Electronics*, Vol. 71, No. 5, 4396–4406, 2024.

[7] Yuan, L., K. Han, C. Zhang, X. Zhu, and Y. Ding, "Comparative analysis of full-order SMO and STM-MRAS in SPMSM sensorless drive system," *IEEE Journal of Emerging and Selected Topics in Power Electronics*, Vol. 12, No. 3, 2592–2603, 2024.

[8] Yang, D., S. Huang, W. Liao, X. Wu, X. Yu, T. Wu, D. Luo, and S. Huang, "ILADRC-based sensorless IPMSM strategy with adaptive harmonic filtering-extended state observer for current quality improvement," *IEEE Transactions on Power Electronics*, Vol. 41, No. 2, 1752–1763, 2026.

[9] Xiao, L., J. Zhang, H. Xie, and C. Hu, "A novel speed estimation algorithm for a permanent magnet linear synchronous motor using an extended kalman filter with multiple fading factors," *IEEE Transactions on Magnetics*, Vol. 60, No. 11, 1–5, 2024.

[10] Caramori, G., I. Oliani, A. S. Lunardi, and A. J. S. Filho, "Robust predictive current control using luenberger observer applied to an induction motor for agricultural electrical traction," *IEEE Access*, Vol. 13, 132 293–132 302, 2025.

[11] Chen, S., X. Yu, X. Wu, C. Li, W. Ding, Y. Xu, J. Zou, D. Lv, and Z. Ma, "A novel computationally efficient finite position set-phase locked loop for low-speed sensorless IPMSM control," *IEEE Transactions on Power Electronics*, Vol. 41, No. 2, 1562–1568, 2026.

[12] Bi, G., Y. Chen, K. Wang, S. Cao, and T. Yang, "Sensorless control design and stability analysis of high-speed dual three-phase permanent motor drive for future aircraft applications," *IEEE Transactions on Power Electronics*, Vol. 40, No. 11, 16 169–16 183, 2025.

[13] Gao, Y., W. Wang, C. Yang, Y. Zhang, T. Qie, and T. Ma, "A new reaching law for anti-disturbance sliding mode control of steer-by-wire system," *IEEE Transactions on Vehicular Technology*, Vol. 74, No. 3, 4064–4075, 2025.

[14] Kumar, S. and B. Singh, "Sensorless super-twisting SMO based PMSM drive with improved DANF-PLL for hybrid three-wheeler EV application," *IEEE Transactions on Industry Applications*, Vol. 61, No. 5, 7362–7371, 2025.

[15] Wang, D. and X. Liu, "Sensorless control of PMSM with improved adaptive super-twisting sliding mode observer and IST-QSG," *IEEE Transactions on Transportation Electrification*, Vol. 11, No. 1, 721–731, 2025.

[16] Yu, M. and Z. Wang, "Sensorless control of permanent magnet synchronous motors based on composite nonlinear functions and ESO-PLLs," *Electrical Engineering*, Vol. 108, No. 1, 46, 2026.

[17] Wang, D., B. Li, and Y. Zhao, "An adaptive SMO approach for low-chattering sensorless control of PMSM," *IEEE Transactions on Power Electronics*, Vol. 40, No. 10, 15 329–15 338, 2025.

[18] Zhang, X., J. Zhu, X. Wu, Z. Zheng, H. Liu, Y. Xue, F. Wan, and H. Zou, "Sensorless control of SPMSM using a full-order super-twisting observer and HR-PI-based FPLL with tunable forward gain," *IEEE Transactions on Power Electronics*, Vol. 40, No. 11, 16 525–16 537, 2025.

[19] Guo, L., W. Xu, N. Jin, and H. Xiao, "A DC-offset removed sensorless control method for PMSM based on SMO with an improved prefilter and a speed immune position error compensation strategy," *IEEE Transactions on Power Electronics*, Vol. 40, No. 4, 5163–5176, 2025.

[20] Hu, J., Z. Wang, H. Wang, and C. He, "Gain compensation-based quasi-resonant PLL with adaptive super-twisting SMO for position error suppression of IPMSM sensorless control," *IEEE Journal of Emerging and Selected Topics in Power Electronics*, Vol. 12, No. 5, 4888–4899, 2024.

[21] Hou, Q., S. Ding, W. Dou, and L. Jiang, "Estimated position error suppression using quasi-super-twisting observer and enhanced quadrature phase-locked Loop for PMSM sensorless drives," *IEEE Transactions on Circuits and Systems II: Express Briefs*, Vol. 71, No. 8, 3865–3869, 2024.

[22] Wang, M. H., Y. X. Xu, and J. B. Zou, "ESO-PLL based position sensorless control of permanent magnet synchronous motor," *Chinese Journal of Electrical Engineering*, Vol. 42, No. 20, 7599–7608, 2022.

[23] Yin, Z., Y. Zhang, X. Cao, D. Yuan, and J. Liu, "Estimated position error suppression using novel PLL for IPMSM sensorless drives based on full-order SMO," *IEEE Transactions on Power Electronics*, Vol. 37, No. 4, 4463–4474, 2022.

[24] Guo, L., Z. Xu, Y. Li, Y. Chen, N. Jin, and F. Lu, "An inductance online identification-based model predictive control method for grid-connected inverters with an improved phase-locked loop," *IEEE Transactions on Transportation Electrification*, Vol. 8, No. 2, 2695–2709, 2022.

[25] Yao, G., Y. Cheng, Z. Wang, and Y. Xiao, "Study on a second-order adaptive sliding-mode observer control algorithm for the sensorless permanent magnet synchronous motor," *Processes*, Vol. 11, No. 6, 1636, 2023.